Understanding Stability of Low-Inertia Systems

Uros Markovic, *Student Member, IEEE,* Ognjen Stanojev, *Student Member, IEEE,*
Evangelos Vrettos, *Member, IEEE,* Petros Aristidou, *Member, IEEE,* and Gabriela Hug, *Senior Member, IEEE*

***Abstract*—A large-scale integration of renewable generation, usually interfaced to the network through power electronics, has led to an overall decrease in power system inertia. This paper presents novel insights on the fundamental stability properties of such systems. For that purpose, a uniform set of Differential-Algebraic Equations (DAEs) describing a generic, low-inertia power system has been developed. A full-order, state-of-the-art control scheme of both synchronous and converter-based generators are included, with the latter differentiating between the *grid-forming* and *grid-following* mode of operation. Furthermore, the dynamics of transmission lines and loads are captured in the model. Using modal analysis techniques such as participation factors and parameter sensitivity, we determine the most vulnerable segments of the system and investigate the adverse effects of the underlying control interference. Finally, the appropriate directions for improving the system stability margin under different generation portfolios have been proposed.**

***Index Terms*—differential-algebraic equations, voltage source converter, synchronous generator, small-signal stability, low-inertia systems**

I. Introduction

In an effort to render the electric power system more sustainable, increasing shares of renewable generation, e.g., wind turbines and solar panels, are being deployed all around the world. Due to physical properties of such units and the fact that they are typically interfaced via Voltage Source Converters (VSCs) to the system, their interaction with the grid is substantially different compared to traditional plants and thus poses many challenges for power system modeling, analysis and control [1]. On the one hand, with the reduction of total system inertia and the associated faster frequency dynamics, the existing protection and under-frequency load shedding schemes are becoming obsolete. On the other, a high penetration of fast-acting VSCs introduces a timescale separation between the corresponding controls of synchronous and converter-based generators, which can adversely affect frequency and voltage stability. With the aim of providing solutions to the underlying problems, detailed and accurate models of low-inertia systems, usually in the form of Differential Algebraic Equations (DAEs), are needed for the purposes of small-signal analysis.

The field of small-signal analysis is well established for conventional power systems [2], [3]. With the increasing integration of renewables, a number of publications addressing modeling and stability of $100\,\%$ inverter-based microgrids has emerged. The focus of these studies differentiates drastically, varying from individual converter operation modes in a single-machine infinite-bus equivalent [4]–[6] to operation of real-size distribution grids [7]–[9]. In contrast, the currently ongoing transition phase towards inertia-less power systems has been somewhat neglected in the literature. Having in mind that operators in Ireland [10], Texas [11] and South Australia [12] are already facing obstacles regarding excessively high wind penetration during certain periods of the day, the fundamental understanding of low-inertia systems and their stability properties is of crucial importance.

The existing literature on power systems with low rotational inertia confines itself to very basic network models and often oversimplified generator control schemes, mostly due to the lack of a uniform state-space formulation for stability analyses. Moreover, the focus is primarily set on distribution networks and microgrids, thus neglecting the potential impact of line dynamics. In [13], the interactions between a VSM-controlled generator and a converter-interfaced load are investigated by considering small-signal stability under different operating conditions. While the authors include a dynamical model of the load and the interconnecting line, they analyze stability only via a basic parameter sweep of the VSM inertia constant and load impedance.

Alternatively, a two-bus microgrid comprised of VSC and Synchronous Generator (SG) was studied in [14] and [15]. The work in [14] considers line dynamics and relatively detailed control structures of both units, but only aims at model validation and the impact of operating points on DAE linearization. On the other hand, the authors in [15] provide insightful remarks regarding the permissible penetration levels of *grid-following* inverters, as well as the relevance of different controllers on small-signal stability. However, they employ an impractical inverter scaling method, which obstructs such DAE implementation on a larger system, and disregard dynamics of the lines. Another limitation of this work lies in oversimplified control schemes, e.g., omittance of Power System Stabilizer (PSS) and important flux dynamics from the SG model. Furthermore, neither of the aforementioned studies employs participation factors for identifying the adverse interactions and determining the true root of instability, nor considers the impact of different converter operation modes.

This study combines the work from [14] and [16], and improves on it in several ways. First, we introduce a uniform, high-fidelity DAE formulation of a generic, low-inertia system that captures all relevant physical properties and associated dynamics, including synchronous and converter-based generators, as well as the dynamics of loads and transmission lines. Second, we highlight the issues related to timescale separation in such systems, and subsequently derive analytic expressions for necessary control criteria pertaining to the impact of transmission line dynamics. Finally, we determine the most vulnerable segments of the system and investigate

This project has received funding from the *European Union's Horizon 2020 research and innovation programme* under grant agreement No 691800. This paper reflects only the authors' views and the European Commission is not responsible for any use that may be made of the information it contains.

the adverse effects of the underlying control interference. As a result, some new insights on the overall stability of low- and no-inertia systems are presented, together with the appropriate directions for improving the system stability margin under different generation portfolios. The remainder of the paper is structured as follows. In Section II, the state-of-the-art converter control scheme is specified. Section III presents the dynamics of a synchronous generator equipped with a prime mover, governor and voltage excitation system. Subsequently, in Section IV the uniform mathematical formulation of the system, as well as the appropriate synchronization and reference frame alignment are elaborated. Furthermore, the associated timescale separation characteristic of low-inertia systems is described. The simulation results from different case studies and the respective stability margins are illustrated in Section V, whereas Section VI draws the main conclusions and discusses the outlook of the study.

II. VSC Control Design

The proposed converter model is based on a state-of-the-art VSC control scheme presented in Fig. 1, where the converter is connected to the system through an RLC filter and a transformer. The outer control loop consists of active and reactive power controllers, which provide the output voltage angle and magnitude reference by adjusting the predefined setpoints according to a measured power imbalance. The reference voltage vector signal is sent to the inner control loop consisting of cascaded voltage and current controllers operating in a Synchronously-rotating Reference Frame (SRF). In order to detect the system frequency at the Point of Common Coupling (PCC), a Phase-Locked Loop (PLL) synchronization unit is included in the model. However, in case of a *grid-forming* converter this unit is bypassed via $\omega_c^* = \omega_0$, with ω_0 being the nominal system frequency.

Complete control is implemented in the internal SRF, with the (abc/dq)-block denoting a sequence of power-invariant Clarke ($\boldsymbol{T}_c$) and Park ($\boldsymbol{T}_p$) transformations from a stationary (abc)-frame to the SRF:

$$\boldsymbol{x}^{dq} = \underbrace{\sqrt{\frac{2}{3}}\begin{bmatrix}\cos\theta & \cos(\theta-\frac{2\pi}{3}) & \cos(\theta+\frac{2\pi}{3})\\ \sin\theta & \sin(\theta-\frac{2\pi}{3}) & \sin(\theta+\frac{2\pi}{3})\end{bmatrix}}_{\boldsymbol{T}_p\boldsymbol{T}_c}\boldsymbol{x}^{abc} \quad (1)$$

It should be noted that the mathematical model is defined in per unit (denoted by lower-case symbols), and the quantities in the (dq)-frame are described in complex space vector form:

$$\boldsymbol{x} \equiv \boldsymbol{x}^{dq} = x^d + jx^q \quad (2)$$

with the dq superscript omitted in the remainder of the paper. Furthermore, the external control setpoints, e.g., the active power reference, are marked with x^*, whereas the internally computed references are represented as $\bar{x}$. A detailed mathematical formulation of the Differential-Algebraic Equation (DAEs) set describing the converter control scheme is presented in the remainder of this section.

A. Electrical Interface and Power Calculation

The electrical system includes an RLC filter (r_f, l_f, c_f) and a transformer equivalent (r_t, l_t) to model the respective copper and iron losses. It is modeled in the SRF defined by the angular frequency ω_c of the converter's Active Power Control (APC). The SRF state-space equations are formulated as follows:

$$\dot{\boldsymbol{i}}_s = \frac{\omega_b}{l_f}(\boldsymbol{v}_m - \boldsymbol{e}_g) - \left(\frac{r_f}{l_f}\omega_b + j\omega_b\omega_c\right)\boldsymbol{i}_s \quad (3)$$

$$\dot{\boldsymbol{i}}_g = \frac{\omega_b}{l_t}(\boldsymbol{e}_g - \boldsymbol{v}_n) - \left(\frac{r_t}{l_t}\omega_b + j\omega_b\omega_c\right)\boldsymbol{i}_g \quad (4)$$

$$\dot{\boldsymbol{e}}_g = \frac{\omega_b}{c_f}(\boldsymbol{i}_s - \boldsymbol{i}_g) - j\omega_c\omega_b\boldsymbol{e}_g \quad (5)$$

where $\boldsymbol{i}_s$ is the switching current flowing through the filter inductance, $\boldsymbol{v}_m$ is the modulation voltage at the converter output, $\boldsymbol{i}_g$ is the current flowing into the grid, $\boldsymbol{e}_g$ is the output voltage across the filter capacitance, and $\boldsymbol{v}_n$ denotes the nodal voltage at the PCC. System base frequency is represented by ω_b and equals the nominal frequency.

The power calculation block computes the active and reactive power output of the converter by processing the measurements of voltage and current after the filter:

$$p_c = \Re(\boldsymbol{e}_g\boldsymbol{i}_g^*) \quad , \quad q_c = \Im(\boldsymbol{e}_g\boldsymbol{i}_g^*) \quad (6)$$

with $\boldsymbol{i}_g^*$ being a complex conjugate of the grid current.

B. Phase-Locked Loop

The synchronization unit is implemented as a Type-2 PLL, which estimates the grid frequency and keeps the VSC synchronized in a *grid-following* mode of operation [17]. It measures the stationary output voltage $\boldsymbol{e}_g$ and transforms it into an internal (dq)-frame, hence introducing a second SRF:

$$\hat{\boldsymbol{e}}_g = \boldsymbol{e}_g e^{-j\vartheta_{pll}} \quad (7)$$

$$\dot{\vartheta}_{pll} = (\omega_{pll} - \omega_c)\omega_b \quad (8)$$

The internally computed output voltage is denoted as $\hat{\boldsymbol{e}}_g$, while ϑ_{pll} is the angle difference between the two SRFs. The synchronization is achieved by diminishing the q-component of $\hat{\boldsymbol{e}}_g$ and thus aligning the d-axis of the internal SRF with the output voltage space vector $\boldsymbol{e}_g$, as described in [6]:

$$\omega_{pll} = \omega_0 + K_p^{pll}\hat{e}_g^q + K_i^{pll}\varepsilon \quad (9)$$

$$\dot{\varepsilon} = \hat{e}_g^q \quad (10)$$

$$\dot{\theta}_{pll} = \omega_{pll}\omega_b \quad (11)$$

The estimated frequency and angle are represented as ω_{pll} and θ_{pll} respectively, whereas ε is an integrator state.

C. Outer Control Loop

The main function of outer control is to generate a voltage phasor reference. This is achieved by adjusting the predefined active and reactive setpoints according to a measured power imbalance. Since the focus of this work is on converter operation on a transmission grid level, both traditional droop and virtual inertia control schemes have been considered for active power regulation.

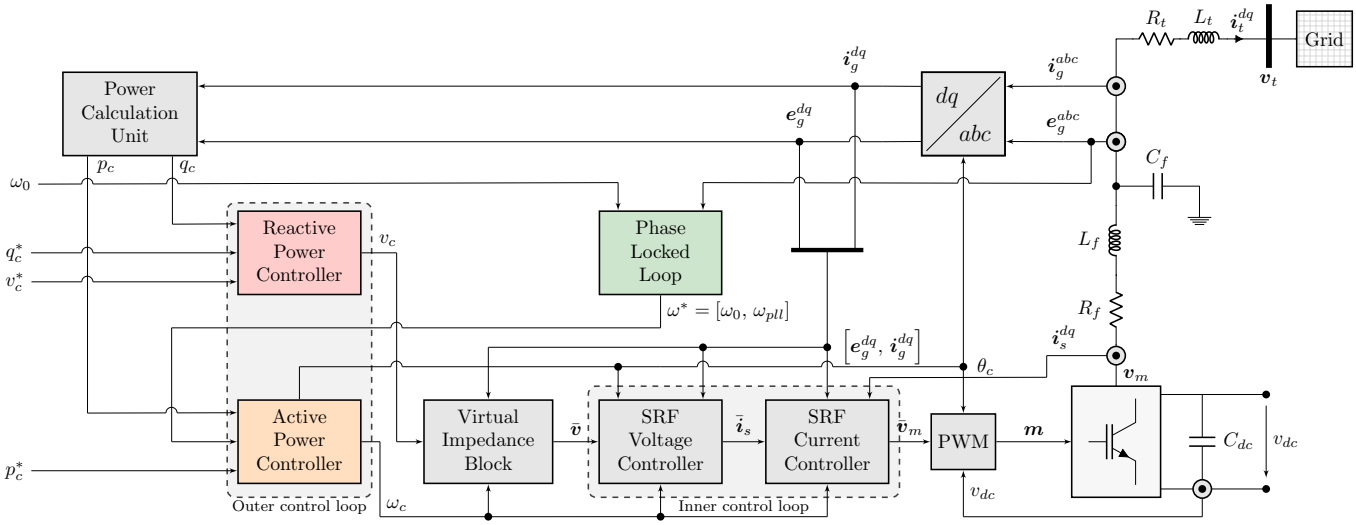

Fig. 1: General configuration of the implemented VSC control structure.

For droop control the measured active power signal is passed through a first-order Low-Pass Filter (LPF) with a cut-off frequency $\omega_z = 2\pi f_z$. Subsequently, the active power droop gain R_p regulates the output frequency ω_c based on the mismatch between the filtered power measurement signal $\tilde{p_c}$ and the external setpoint p_c^*, as follows:

$$\omega_c = \omega_c^* + R_p(p_c^* - \tilde{p_c}) \tag{12}$$
$$\dot{\tilde{p_c}} = \omega_z(p_c - \tilde{p_c}) \tag{13}$$

On the other hand, the virtual inertia is based on a linearized form of the conventional swing equation, representing the relation between physical inertia and damping of a synchronous machine [18], [19]. Hence, the frequency can be expressed via a differential equation of the form:

$$\dot{\omega}_c = \frac{1}{M_c}\underbrace{(p_c^* - p_c)}_{p_m - p_e} - \frac{1}{M_c}\underbrace{D_c(\omega_c - \omega_c^*)}_{p_d} \tag{14}$$

where the mechanical (p_m) and electrical (p_e) power of a synchronous machine are replaced by the active power setpoint p^* and the converter output power p_c, respectively. The damping power term p_d is incorporated through a feedback loop, with a damping constant D_c being the feedback gain imposed on the frequency mismatch, while a normalized inertia constant M_c determines the initial RoCoF during transients. The two control architectures can be proven mathematically equivalent under certain steady-state conditions [4], as follows:

$$M_c = \frac{1}{\omega_z R_p} \quad , \quad D_c = \frac{1}{R_p} \tag{15}$$

Nonetheless, virtual inertia control offers overall better behavior during frequency transients [20]. Furthermore, the corresponding phase angle θ_c is used as a reference angle for the (dq)-transformation of the entire converter control system, with exclusion of the PLL, i.e., $\dot{\theta}_c = \omega_c \omega_b$.

Analogous to APC, the strong coupling of reactive power and voltage enables a droop-based implementation of Reactive Power Control (RPC). The desired output voltage v_c is computed as an adjustment of the voltage setpoint v^* according to a mismatch in the reactive power:

$$v_c = v_c^* + R_q(q_c^* - \tilde{q_c}) \tag{16}$$
$$\dot{\tilde{q_c}} = \omega_z(q_c - \tilde{q_c}) \tag{17}$$

with q_c, $\tilde{q_c}$ and q_c^* denoting the actual, LPF and setpoint value of the reactive power, respectively, and R_q being the reactive power droop gain.

D. Virtual Impedance

Virtual impedance is embedded as an additional degree of freedom for active stabilization and disturbance rejection, as it splits the voltage reference into (dq)-components before passing it to the inner control loop. Despite maximizing the active power output when set to zero, a non-zero q-component is necessary to allow for "acceleration" and "deceleration" of the virtual machine [21]. Therefore, a minor cross-coupling of d- and q-components is included via the resistive (r_v) and inductive (l_v) elements. While the former is set to $r_v = 0$ for simplicity, the latter should be kept as small as possible, yielding the respective d-axis and q-axis voltage components:

$$\bar{v}_c^d = v_c - r_v i_g^d + \omega_c l_v i_g^q \tag{18}$$
$$\bar{v}_c^q = -r_v i_g^q + \omega_c l_v i_g^d \tag{19}$$

which are directly used as reference inputs for the decoupling SRF voltage controller.

E. Inner Control Loop and Modulation

The computed voltage and frequency references are passed to the inner control loop in order to impose a controlled saturation of the converter's currents and voltages [22].

A structure of the SRF voltage controller follows the similar principles as the controllers in [4], [22]:

$$\bar{\boldsymbol{i}}_s = K_p^v(\bar{\boldsymbol{v}} - \boldsymbol{e}_g) + K_i^v \boldsymbol{\xi} + j\omega_c c_f \boldsymbol{e}_g + K_f^i \boldsymbol{i}_g \tag{20}$$
$$\dot{\boldsymbol{\xi}} = \bar{\boldsymbol{v}} - \boldsymbol{e}_g \tag{21}$$

TABLE I: Converter Control Parameters

Parameter	Symbol	Value	Unit
Active power droop gain	R_p	2	%
Reactive power droop gain	R_q	0.1	%
LPF cut-off frequency	f_z	5	Hz
RLC filter resistance	r_f	0.03	p.u.
RLC filter inductance	l_f	0.08	p.u.
RLC filter capacitance	c_f	0.074	p.u.
P-gain of SRF current control	K_p^i	0.74	-
I-gain of SRF current control	K_i^i	1.19	-
FF-gain of SRF current control	K_f^i	1	-
P-gain of SRF voltage control	K_p^v	0.52	-
I-gain of SRF voltage control	K_i^v	1.16	-
FF-gain of SRF voltage control	K_f^v	1	-
PLL proportional gain	K_p^{pll}	0.4	-
PLL integral gain	K_i^{pll}	4.69	-
Virtual impedance resistance	r_v	0	p.u.
Virtual impedance inductance	l_v	0.2	p.u.

where K_p^v and K_i^v are the proportional and integral gains of the SRF voltage PI controller, and $\boldsymbol{\xi}$ is the integrator state. Furthermore, a feed-forward signal of the measured currents can be enabled or disabled by changing the gain $K_f^i \in [0,\, 1]$. The output current reference $\bar{\boldsymbol{i}}_s$ is then used as an input setpoint to the current controller.

Similar to its voltage counterpart, the configuration of the SRF current controller is based on a PI control with decoupling terms:

$$\bar{\boldsymbol{v}}_m = K_p^i(\bar{\boldsymbol{i}}_s - \boldsymbol{i}_s) + K_i^i\boldsymbol{\gamma} + j\omega_c l_f \boldsymbol{i}_s + K_f^v \boldsymbol{e}_g \tag{22}$$

$$\dot{\boldsymbol{\gamma}} = \bar{\boldsymbol{i}}_s - \boldsymbol{i}_s \tag{23}$$

with K_p^i, K_i^i and K_f^v being the respective controller gains, and $\boldsymbol{\gamma}$ the integrator state. The generated output voltage reference $\bar{\boldsymbol{v}}_m$ is used to determine the averaged modulation signal

$$\boldsymbol{m}^{abc} = (\boldsymbol{T}_p\boldsymbol{T}_c)^{-1}\,\boldsymbol{m}^{dq} = (\boldsymbol{T}_p\boldsymbol{T}_c)^{-1}\,\frac{\bar{\boldsymbol{v}}_m}{v_{dc}} \tag{24}$$

which reduces the AC side sensitivity to DC voltage (v_{dc}) oscillations [4]. Due to high complexity and very fast internal dynamics, the converter switching and DC-side buffers are not included in the model, since their impact on the small-signal stability is rather negligible.

With inclusion of the current and voltage dynamics associated to the electrical system interface in (3)-(5), the complete mathematical model consists of 13 states for the *grid-forming* and 15 states for the *grid-following* converter unit. All relevant converter parameters used in this paper are presented in Table I, whereas more details on the overall converter control structure, potential operation modes and respective transient properties can be found in [5], [6], [20].

III. Synchronous Generator Model

We consider a traditional two-pole synchronous generator equipped with a prime mover and a governor, described in per unit. Additionally, a voltage excitation system consisted of Automatic Voltage Regulator (AVR) and PSS is incorporated. A detailed block diagram is showcased in Fig. 2, where the synchronous generator is connected to the grid trough a transformer. The main parameters are listed in Table II. This is a well-established configuration used both for academic and industrial purposes [2], [23], [24].

A. Electrical Interface

A synchronous generator is interfaced through a transformer (r_t, l_t) to the grid, and modeled in the SRF defined by its synchronous velocity ω_s:

$$\dot{\boldsymbol{i}}_s = \frac{\omega_b}{l_t}(\boldsymbol{e}_s - \boldsymbol{v}_n) - \left(\frac{r_t}{l_t}\omega_b + j\omega_b\omega_s\right)\boldsymbol{i}_s \tag{25}$$

with $\boldsymbol{e}_s$ and $\boldsymbol{i}_s$ denoting the stator voltage and current respectively, and $\boldsymbol{v}_n$ representing the nodal voltage at the PCC.

B. Internal Machine Dynamics

The internal machine dynamics are characterized by the transients in the rotor circuits, as transients in the stator windings decay rapidly and can thus be neglected. Rotor

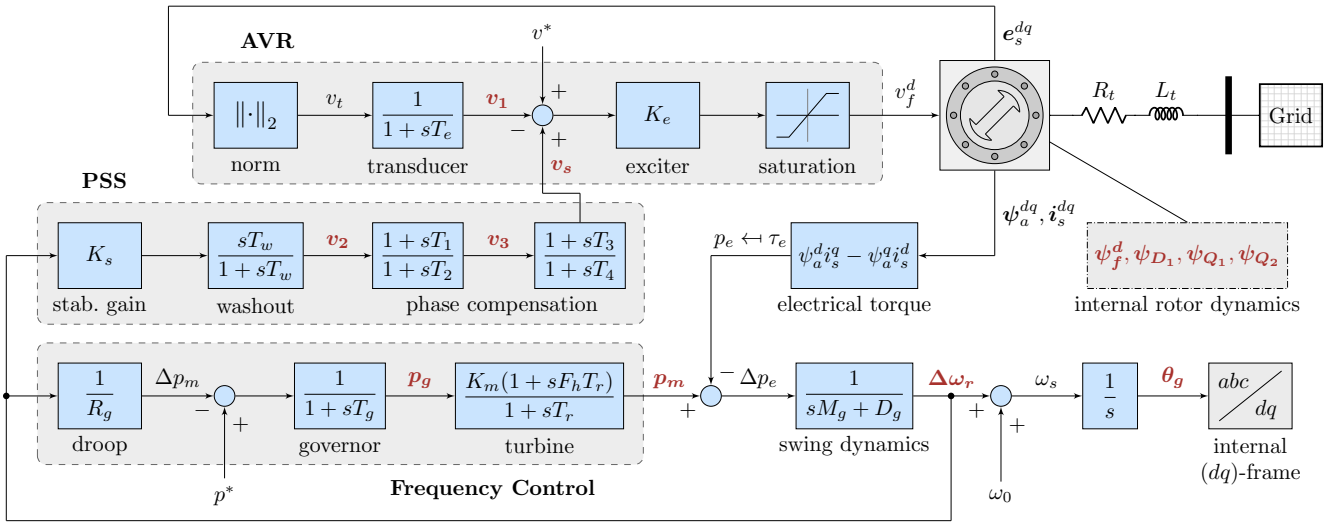

Fig. 2: Block diagram of a synchronous generator equipped with a prime mover, governor and voltage excitation system.

TABLE II: Synchronous Generator Parameters

Parameter	Symbol	Value	Unit
Droop control gain	R_g	2	%
Governor time constant	T_g	0.5	s
Reheat time constant	T_r	10	s
Mechanical power gain factor	K_m	0.85	-
Turbine power fraction factor	F_h	0.1	-
Normalized inertia constant	M_g	13	s
Normalized damping factor	D_g	1	p.u.
Transducer time constant	T_e	0.05	s
AVR exciter control gain	K_e	200	-
Saturation minimum output	$V_f^{\min}$	0	p.u.
Saturation maximum output	$V_f^{\max}$	4	p.u.
PSS stabilization gain	K_s	5	-
Washout time constant	T_w	2	s
1st lead-lag derivative time constant	T_1	0.25	s
1st lead-lag delay time constant	T_2	0.03	s
2nd lead-lag derivative time constant	T_3	0.15	s
2nd lead-lag delay time constant	T_4	0.015	s

dynamics originate in the armature reaction, i.e., in the effect of the stator field on the rotor currents, which can be described through flux linkage dynamics:

$$\dot{\psi}_f^d = \frac{\omega_0 r_f}{x_{a,u}^d} v_f^d - \frac{\omega_0 r_f}{x_f}\left(\psi_f^d - \psi_a^d\right) \tag{26a}$$

$$\dot{\psi}_{D_1} = -\frac{\omega_0 r_{D_1}}{x_{D_1}}\left(\psi_{D_1} - \psi_a^d\right) \tag{26b}$$

$$\dot{\psi}_{Q_1} = -\frac{\omega_0 r_{Q_1}}{x_{Q_1}}\left(\psi_{Q_1} - \psi_a^q\right) \tag{26c}$$

$$\dot{\psi}_{Q_2} = -\frac{\omega_0 r_{Q_2}}{x_{Q_2}}\left(\psi_{Q_2} - \psi_a^q\right) \tag{26d}$$

Here, subscripts f, D_1, Q_1 and Q_2 stand for the quantities of the field circuit, d-axis damping circuit and two q-axis damping circuits respectively, whereas ψ, r and x denote the respective flux linkage, resistance and reactance of a circuit; v_f is the exciter output voltage, ω_0 designates the synchronous angular velocity, and $x_{a,u}^d$ stands for the unsaturated mutual reactance. Superscripts d and q are omitted from damping circuit quantities for simplicity. The armature flux linkages are expressed as follows:

$$\psi_a^d = \hat{x}_{a,s}^d\left(-i_s^d + \frac{\psi_f^d}{x_f} + \frac{\psi_{D_1}}{x_{D_1}}\right) \tag{26e}$$

$$\psi_a^q = \hat{x}_{a,s}^q\left(-i_s^q + \frac{\psi_{Q_1}}{x_{Q_1}} + \frac{\psi_{D_1}}{x_{Q_2}}\right) \tag{26f}$$

with the subtransient, saturated, mutual reactances $\hat{x}_{a,s}^d$ and $\hat{x}_{a,s}^q$ defined in the form:

$$\hat{x}_{a,s}^d = \left(\frac{1}{x_{a,s}^d} + \frac{1}{x_f} + \frac{1}{x_{D_1}}\right)^{-1} \tag{26g}$$

$$\hat{x}_{a,s}^q = \left(\frac{1}{x_{a,s}^q} + \frac{1}{x_{Q_1}} + \frac{1}{x_{Q_2}}\right)^{-1} \tag{26h}$$

Finally, the inclusion of stator circuit balance completes the set of differential-algebraic equations in (26) describing the internal generator dynamics:

$$e_s^d = -r_a i_s^d + x_l i_s^q - \psi_a^q \tag{26i}$$

$$e_s^q = -r_a i_s^q + x_l i_s^d - \psi_a^d \tag{26j}$$

Stator voltages and currents are denoted by $\boldsymbol{e}_s^{dq}$ and $\boldsymbol{i}_s^{dq}$, while r_a and x_l represent the armature resistance and leakage reactance respectively. Combining (25)-(26) with 8 controller states depicted in Fig. 2 yields a 14th order model. For more details regarding the generator modeling and internal parameter computation we refer the reader to [2].

IV. Uniform Power System Formulation

A. Network Modeling

Modeling of the transmission network is described for a generic system depicted in Fig. 3, composed of generators supplying local RL loads and the interconnecting transmission lines modeled as π-sections. In order to establish a consistent mathematical formulation, all variables have to be defined within a single, uniform SRF. For this purpose, the terminal currents (i_{t_u}) and voltages (v_{t_u}) of each generator unit $u \in \mathcal{U}$ are mapped to the network nodes $j \in \mathcal{J}_u \subset \mathcal{J}$ with generator connection, and subsequently aligned to the network SRF rotating at nominal angular speed ω_n:

$$\boldsymbol{x}_{n_j} = \boldsymbol{x}_{t_u} e^{-j(\theta_n - \theta_j)},\ \forall j, u \tag{27}$$

where $\boldsymbol{x}_{n_j} \in \{\boldsymbol{i}_{n_j}, \boldsymbol{v}_{n_j}\}$ denotes the "nodal" metrics described in the nominal reference frame, $\dot{\theta}_n = \omega_n \omega_b$ is the uniform SRF angle, and θ_j corresponds to the internal SRF angle of the respective unit, i.e., θ_s for the synchronous and θ_c for the converter-based generator. Several benefits of using a uniform reference frame for describing the power system dynamics have already been indicated in [25]. The nodal voltage and current dynamics can now be expressed as follows:

$$\dot{\boldsymbol{v}}_{n_j} = \frac{\omega_b}{c_{l_j}} \boldsymbol{i}_{c_j} - j\omega_n \omega_b \boldsymbol{v}_{n_j},\ \forall j \tag{28}$$

$$\dot{\boldsymbol{i}}_{l_j} = \frac{\omega_b}{l_{l_j}} \boldsymbol{v}_{n_j} - \left(\frac{r_{l_j}}{l_{l_j}\omega_b} + j\omega_b\omega_n\right) \boldsymbol{i}_{l_j},\ \forall j \tag{29}$$

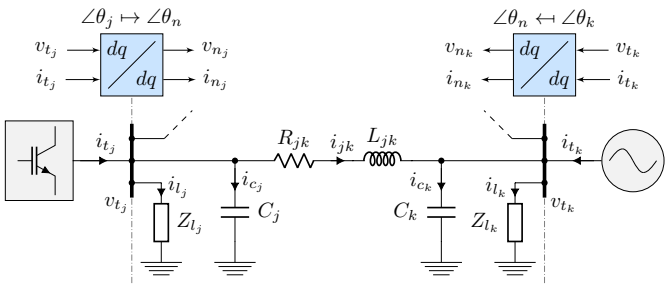

Fig. 3: Generic network model with line dynamics and the respective (dq)-frame alignment.

thus capturing the load (r_{l_j}, l_{l_j}) and aggregate shunt (c_j) phenomena at each node $j \in \mathcal{J}$. Finally, the line dynamics are represented using a conventional RL circuit formulation:

$$\dot{\boldsymbol{i}}_{jk} = \frac{\omega_b}{l_{jk}}(\boldsymbol{v}_{n_j} - \boldsymbol{v}_{n_k}) - \left(\frac{r_{jk}}{l_{jk}}\omega_b + j\omega_b\omega_n\right)\boldsymbol{i}_{jk},\ \forall j,k \quad (30)$$

with (r_{jk}, l_{jk}) being the respective line parameters and $k \in \mathcal{K}_j$ denoting the set of nodes adjacent to node j. Combining equations (27)-(30) with the algebraic current balance terms at each node in the system completes the DAE formulation.

It should be noted that for the purposes of the small-signal model the alignment in (27) has to be modified, i.e., the frequency at which the uniform SRF rotates must be a state variable instead of a constant ω_n. The reason lies in the linearization of the exponential term performing the rotation, which otherwise gets oversimplified and cannot capture the alignment accurately. As a result, the linearized model is expressed in an SRF of an arbitrary *grid-forming* inverter or a synchronous generator.

B. Uniform Linearized Model

A full state-space form of the VSC control scheme can be derived from (1)-(24), resulting in the 15^{th} order model:

$$\boldsymbol{x}_c = \left[\boldsymbol{e}_g^{dq},\ \boldsymbol{i}_g^{dq},\ \boldsymbol{i}_s^{dq},\ \boldsymbol{\xi}^{dq},\ \boldsymbol{\gamma}^{dq},\ \varepsilon,\ \vartheta_c,\ \vartheta_{pll},\ \tilde{p},\ \tilde{q}\right]^T \quad (31)$$

$$\boldsymbol{u}_c = [p^*,\ q^*,\ v^*, \omega_0]^T \quad (32)$$

where $\boldsymbol{x}_c$ and $\boldsymbol{u}_c$ denote the state and input vectors respectively. For a *grid-forming* inverter the PLL states $(\varepsilon, \vartheta_{pll})$ would be omitted from (31), whereas in case of a virtual inertia APC the state $\tilde{p}$ is replaced by ν_{apc}, as explained in Section II-C. The input vector consists of the converter control setpoints. On the other hand, the 14^{th} order state-space model of a synchronous generator is formulated as follows:

$$\boldsymbol{x}_s = \left[\boldsymbol{i}_s^{dq},\ \boldsymbol{\psi}_s,\ v_1,\ v_2,\ v_3,\ v_s,\ p_g,\ p_m,\ \Delta\omega_r,\ \theta_g\right]^T \quad (33)$$

$$\boldsymbol{u}_s = [p^*,\ v^*]^T \quad (34)$$

with $\boldsymbol{\psi}_s = [\psi_f^d, \psi_{D_1}, \psi_{Q_1}, \psi_{Q_2}]$ being the vector of fluxes describing the internal rotor dynamics. The grid state representation is described by the vector

$$\boldsymbol{x}_g = \left[\boldsymbol{u}_{n_1}, \ldots, \boldsymbol{u}_{n_{N_n}},\ \boldsymbol{i}_{l_1}, \ldots, \boldsymbol{i}_{l_{N_n}},\ \boldsymbol{i}_{b_1}, \ldots, \boldsymbol{i}_{b_{N_b}}\right]^T \quad (35)$$

where N_n and N_b denote the total number of nodes and branches in the network respectively, and $\boldsymbol{i}_{b_m}$ corresponds to the branch currents $\boldsymbol{i}_{jk}$ introduced in (30). Finally, the uniform system formulation can be established:

$$\boldsymbol{x} = \left[\boldsymbol{x}_{c_1}^T, \ldots, \boldsymbol{x}_{c_{N_c}}^T,\ \boldsymbol{x}_{s_1}^T, \ldots, \boldsymbol{x}_{s_{N_s}}^T,\ \boldsymbol{x}_g^T\right]^T \quad (36)$$

$$\boldsymbol{u} = \left[\boldsymbol{u}_{c_1}^T, \ldots, \boldsymbol{u}_{c_{N_c}}^T,\ \boldsymbol{u}_{s_1}, \ldots, \boldsymbol{u}_{s_{N_s}}^T\right]^T \quad (37)$$

with N_s and N_c representing the total number of synchronous and converter-based generators. The small-signal model is thus defined in the general form as

$$\Delta\dot{\boldsymbol{x}} = \boldsymbol{A}\Delta\boldsymbol{x} + \boldsymbol{B}\Delta\boldsymbol{u} \quad (38)$$

where Δ indicates a small-signal deviation around the linearization point $(\boldsymbol{x}_0,\ \boldsymbol{u}_0)$.

C. Timescale Separation

The overall complexity of dynamics pertaining to low-inertia systems is well described through timescale separation illustrated in Fig. 4. Traditional power systems based on synchronous generators have a distinct difference in time constants between the frequency and voltage regulation, with turbines $(T_r \approx 10\,\text{s})$ and governors $(T_g \approx 1\,\text{s})$ operating on a much higher timescales than the exciter $(T_e \approx 50\,\text{ms})$. Considering that the time constants of the line dynamics vary in the $T_l \in [1 - 30]$ ms range, depending on the network type, it is clear that the conventional control schemes would ensure system stability. However, with the inclusion of fast-acting, converter-based generation, the system dynamics become more convoluted. More precisely, the time constants of the PI controllers and LPFs associated with the inner and outer inverter control loops are one or two orders of magnitude smaller than the ones of the synchronous machines, potentially resulting in adverse control interference and instability, especially under high installation share of renewables. Moreover, the time delays associated with Wide Area Monitoring Systems (WAMS) would make any type of centralized system regulation without the use of high-speed fibre optics obsolete.

Another insightful observation is that the impact of network line dynamics becomes more profound in *inertialess* systems. Its effect on frequency stability can be illustrated by analyzing a uniform frequency control loop of an individual *grid-forming*

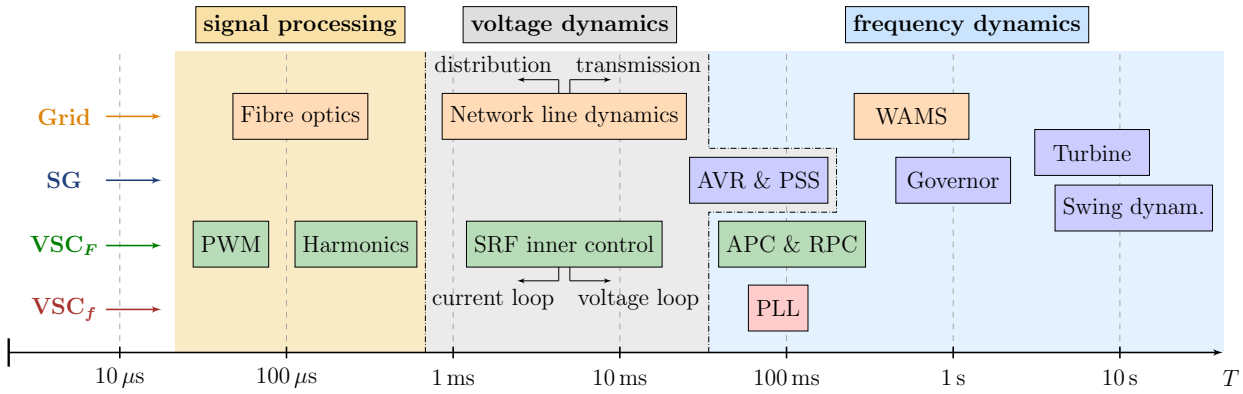

Fig. 4: Timescale separation between different physical and control dynamics in a low inertia system.

inverter connected to $k \in \mathcal{K}_j$ adjacent inverter units described in Appendix A:

$$\tau_z \ddot{\theta}_{c_j} + \left(1 - \omega_b R_p B'_j\right) \dot{\theta}_{c_j} + \omega_b R_p B_j \theta_{c_j} + C_j = 0 \quad (39)$$

with

$$C_j = \omega_b \omega^*_{c_j} + \omega_b R_p p^*_{c_j} \quad (40)$$

$$B_j = \sum_{k \in \mathcal{K}_j} \frac{\omega_0 l_{jk}}{\left(r^2_{jk} + \omega^2_0 l^2_{jk}\right)^2}, \; B'_j = \sum_{k \in \mathcal{K}_j} \frac{2 r_{jk} l^2_{jk}}{\left(r^2_{jk} + \omega^2_0 l^2_{jk}\right)^2}$$

In order to preserve system synchronization the natural negative feedback terms for θ_{c_j} and $\dot{\theta}_{c_j}$ must be positive, indicating an upper limit on the active power droop gain of $R_p < (\omega_b B'_j)^{-1}$. One can notice that such threshold is even more restrictive for a distribution network, due to shorter node distances and a lower l_{jk}/r_{jk} line impedance ratio. Furthermore, the impact of the power network also pertains to inverter synchronization through θ_{cj} term, since very high feedback control gains $\kappa_j = \omega_b R_p B_j$ might lead to inverter frequency oscillations exciting the oscillatory modes of the transmission lines. In other words, the inverters achieve synchronization by inferring information about the phase angle differences through local measurements of currents and voltages. Therefore, the time constant of the transmission lines can be interpreted as a propagation delay of the information on the phase angles, and the controllers cannot act faster than the time needed to observe information through the network. Hence, larger time constants require a lower feedback gain, which implies that shortening or adding transmission lines can make a low-inertia system unstable. Similar remarks have been pointed out for microgrids consisted solely of inverters based on droop [26] and dispatchable virtual oscillator control [27]. While we solely focus on frequency dynamics in this example, it should be noted that the voltage stability could also be assessed using the proposed approach, as indicated in [26]–[28].

V. Results

A. Model Verification

In order to validate the proposed control structure, a nonlinear inverter model was developed in MATLAB Simulink, with the use of a Simscape Power Systems library for the electrical system design. Subsequently, the response to a 10% step change in active power setpoint was compared against the detailed DAE and small-signal models. The results presented in Fig. 5 verify the accuracy of the proposed mathematical formulation, with the small-signal model having better initialization behavior due to aforementioned linearization.

B. Unit Interactions in a 2-bus Test System

For the first case study we consider a simple 2-bus system similar to the one described in Fig. 3, with two generators connected over a transmission line and an RL load supplied at the first node. The goal is to incorporate different units into the system and investigate their dynamic interactions and the respective stability margins. In order to confine the observed phenomena solely to the generators under study, the transmission line dynamics are not taken into account at this point.

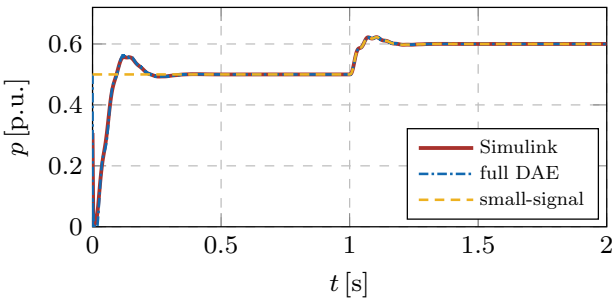

Fig. 5: Transient response of different inverter models to a step change in active power setpoint.

We investigate three different scenarios based on the generator type configuration: (i) a synchronous generator and a *grid-following* VSC; (ii) a synchronous generator and a *grid-forming* VSC; (iii) a *grid-forming* and a *grid-following* VSC. Furthermore, we introduce a penetration ratio η, which describes the installed penetration level of inverter-based units. In first two cases this corresponds to $\eta = p_c/(p_g + p_c)$, whereas in the last scenario this factor denotes the penetration of the *grid-following* generation, i.e., $\eta = p_{c_f}/(p_{c_F} + p_{c_f})$, with subscripts F and f representing the *grid-forming* and *grid-following* converters respectively. The second formulation is justified by *grid-following* units being the main origin of instability, especially under a high installation share.

The stability margins of different system configurations are illustrated in Fig. 6, where the stability is assessed through real-part movement of the most critical eigenvalue $\hat{\lambda}$. Understandably, the system comprising of both synchronous generators and *grid-forming* inverters can withstand drastically higher levels of PE-based devices ($\approx 79\%$), as the voltage phasors at both nodes are fully established and controlled by the local generators. Additionally, the synchronization and power sharing properties are inherently provided by both units. On the other hand, the penetration of *grid-following* generation adversely affects the system balance, and significantly reduces the maximum admissible ratio to $\eta_{\text{max}} \approx 60\,\%$ and $\eta_{\text{max}} \approx 59\,\%$ for Scenarios 2 and 3, respectively. The latter configuration also has a steeper progression of $\hat{\lambda}$, indicating that the penetration ratio can hardly be improved.

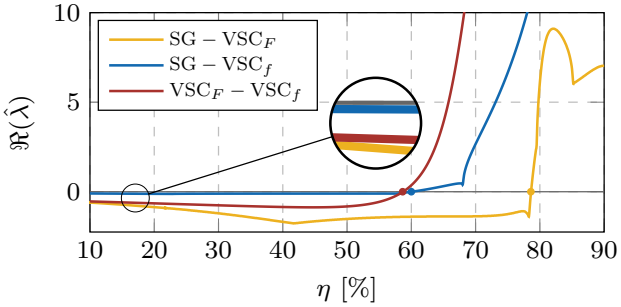

Fig. 6: Impact of inverter penetration on system stability for different unit configuration.

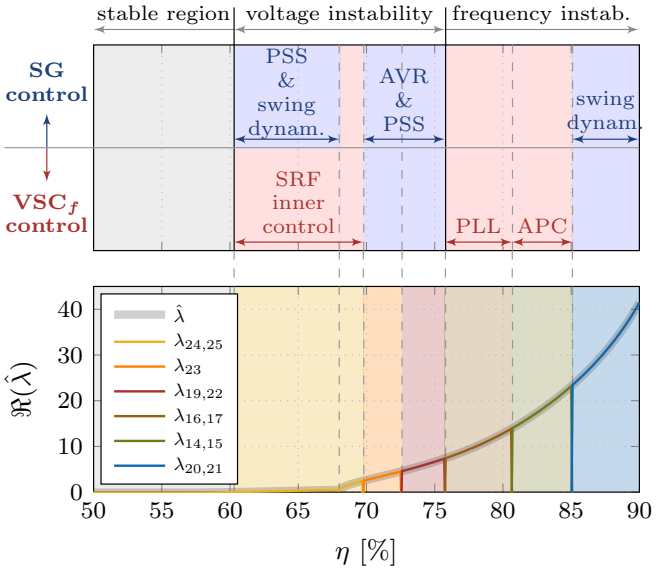

Fig. 7: Impact of different controllers on system stability under high *grid-following* inverter penetration in Scenario I.

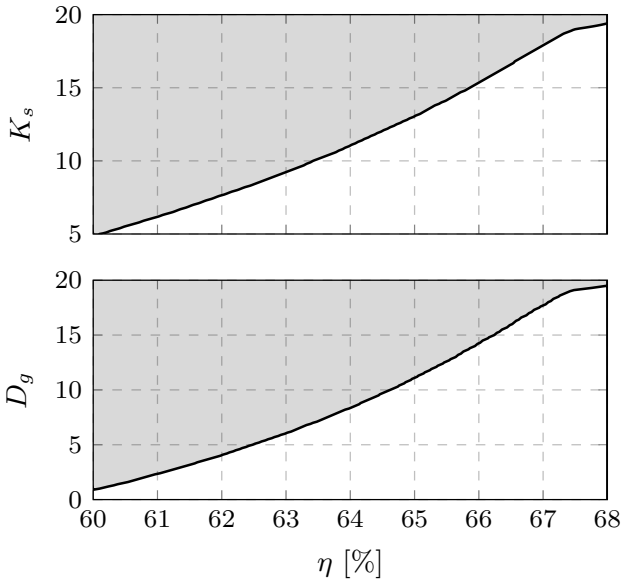

Fig. 8: Stability maps in the $K_s - \eta$ and $D_g - \eta$ planes indicating the effect of PSS stabilization gain and synchronous generator damping on admissible penetration of *grid-following* inverter units in Scenario I.

As a second step, we thoroughly explore the fundamental components contributing to the aforementioned instability. This is achieved by determining the critical modes of the system, employing participation factor and parameter sensitivity analyses, and determining the states, i.e., the controllers, that mainly contribute to such modes. Each of the proposed scenarios comprises a unique DAE system with specific dynamics. Therefore, all three system configurations are individually investigated and elaborated in detail below:

1) Scenario I: It is observed that the inverter penetration above $60\,\%$ leads to system collapse. Interestingly, the instability initially originates in the voltage dynamics, with the VSC inner control loop interfering with the generator's PSS, as illustrated in Fig. 7. Subsequently, the vulnerability spreads across the whole excitation system, including the AVR. At this point the system is heavily unstable. This phenomena comes from the time constants of the inner loops being drastically smaller than the ones of the exciter. More specifically, once the system becomes predominantly PE-based, the "non-forming" aspect of the inverter's voltage phasor diminishes the voltage at the SG terminal and weakens the system resilience. For even higher VSC penetration levels ($> 75\,\%$) the system faces frequency stability issues, as the PLL, and subsequently the active power controller, cannot provide adequate synchronization of the *grid-following* units due to insufficiently strong global frequency signal.

By studying the movement of the critical eigenvalue spectrum in Fig. 7 we can notice that the real part $\Re(\hat{\lambda})$ significantly increases for inverter shares above $68\,\%$. Considering that PSS and converter SRF controllers largely participate in critical modes for $\eta \in [60, 68]$ %, one can assume that tuning the respective control gains could restore system stability within this range. While the increase in stabilization gain K_s shown in Fig. 8 proves to be beneficial for the system, the adjustment of inner loop PI controllers has no impact on the eigenvalue spectrum. This is an expected outcome due to a large timescale separation between the two feedback loops, which in turn hinders the synchronous generation in providing a stiff voltage at the terminal. Furthermore, the SRF converter control is often predefined by the manufacturer and optimally designed for providing fast and accurate voltage and power reference tracking, implying that any parameter changes would distort its original purpose and effectiveness. Beside the SG voltage regulators, the dynamics of the swing equation also prove to be relevant for the overall stability. However, in contrast to the popular belief that low inertia levels lead to vulnerability, it is in fact the insufficient damping D_g that propagates the problem. Similar to the K_s gain, the higher damping constant facilitates the integration of converters, whereas the inertia constant M_g has no impact on the overall penetration. Nonetheless, damping is related to physical properties of synchronous generators, while droop gains, essentially corresponding to damping, are prescribed within narrow ranges by the grid codes. This suggests that the most viable and practical solution would be to improve the PSS design, i.e., increase its responsiveness, in order to accommodate a high penetration of *grid-following* inverter-based generation.

2) Scenario II: As highlighted in the previous scenario, the issues pertaining to the timescale separation between different voltage controllers remain. It can be noticed that the "forming" inverter property bolsters the voltage vector at the respective bus and drastically improves the stability margin of the system. Nonetheless, for $\eta > 78\,\%$ the AVR and PSS controllers cannot achieve adequate voltage stabilization, as the eigenvalues depicted in Fig. 9 drive deeply into the right-hand side of the root loci spectrum. Hence, the maximum feasible penetration of VSCs can hardly be improved upon. Another important

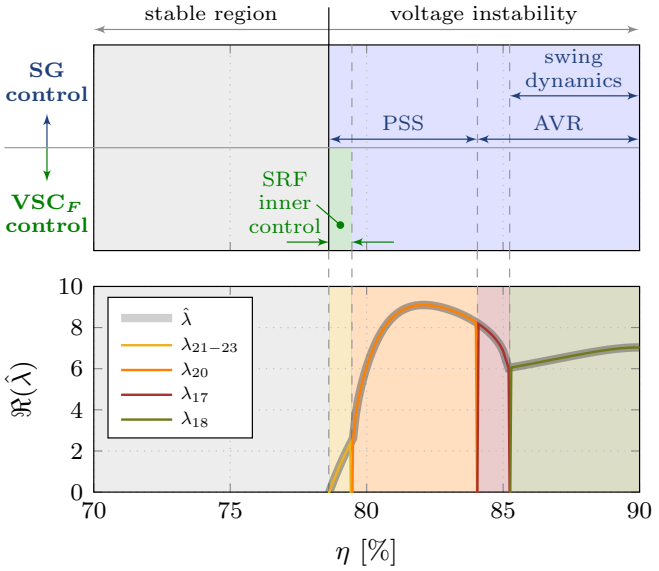

Fig. 9: Impact of different controllers on system stability under high *grid-forming* inverter penetration in Scenario II.

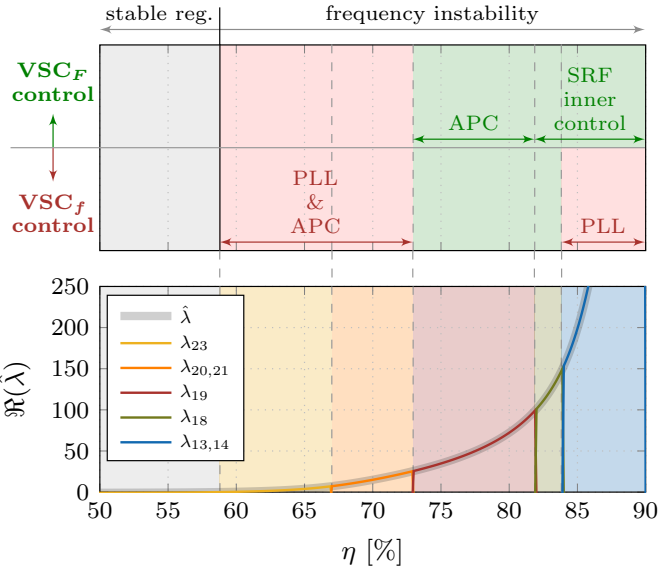

Fig. 10: Impact of different controllers on system stability under high *grid-following* inverter penetration in Scenario III.

observation is that the frequency dynamics are not contributing to instability anymore, since both units independently establish an adequate frequency signal and subsequently synchronize.

3) Scenario III: We tackle the 100 % PE-based scenario by increasing the share of *grid-following* units through factor η, as presented in Fig. 10. The main distinction of this scenario is the elimination of voltage control issues in the presence of SGs and inverters, as both VSCs regulate voltage on the same timescale. In spite of improving the voltage stability of the system, the synchronization problems are aggravated due to an exclusion of a synchronous generator. In other words, the dedicated "forming" capability of a *grid-forming* converter is inferior to the one of a traditional generator. As a result, for penetration levels above $\approx$ 59 % the PLL units of *grid-following* inverters cannot accurately estimate the frequency signal, leading to the failure in the active power control and preventing the system-level synchronization. Similar properties are also reflected in Fig. 11, where a stability map in the $K_p^{pll} - \eta$ plane is depicted. One can observe that a more responsive PLL could potentially facilitate a higher penetration factor η. Nonetheless, this approach does not solve the fundamental problem at hand, and provides only a marginal improvement of few percent. It should be noted that the integral gain of the respective PI controller does not affect the system stability margin, indicating that the original PLL time constant could be maintained in the process.

C. Inclusion of Transmission Line Dynamics

We broaden the scope of our analysis by including the transmission line dynamics described in Section IV. The same three scenarios are re-evaluated and compared against the previous case study, with the respective results illustrated in Fig. 12. A noticeable difference in the stability margin of a 100 % inverter-based system can be observed, where the inclusion of line dynamics significantly broadens the maximum penetration ratio η. This can be justified by the inductive and capacitive components of the lines acting as energy buffers and augmenting the synchronization between the two units, as previously described in Section IV-C. More precisely, the frequency issues associated to a large proportion of PLL-based generation are alleviated through interactions with the LC segments of the transmission lines, which slows down the frequency dynamics and enables the *grid-following* VSCs to more accurately detect the weak, global frequency signal. Similar conclusions have been drawn in [27] for a specific class of *grid-forming* inverters, as well as in [3] using a mechanical analogue of swings in a multi-machine system.

On the other hand, the scenarios experiencing voltage instability problems are for the most part unaffected by the transmission lines. The voltage control interaction between the synchronous and PE-based generation is somewhat mitigated, due to the time constants of the line dynamics and the SRF inner control loops being of the same order of magnitude. However, the line dynamics do not have any impact on the slower modes associated to the synchronous machines. Therefore, the stability in Scenario I cannot be preserved for the *grid-following* penetration above 70 %, as it is associated

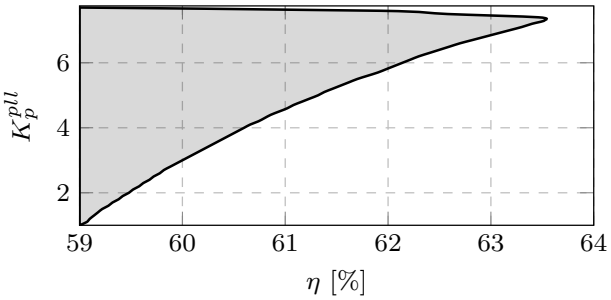

Fig. 11: Stability map in the $K_p^{pll} - \eta$ plane indicating the effect of proportional PLL gain on admissible penetration of *grid-following* inverter units in Scenario III.

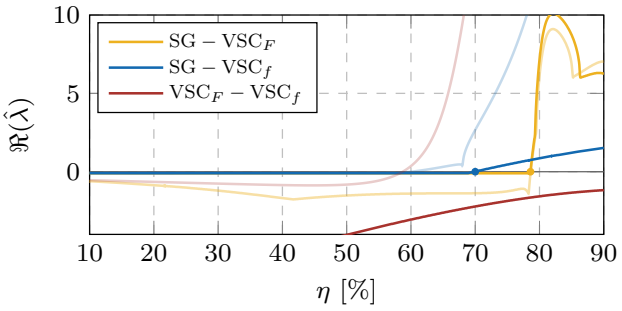

Fig. 12: Impact of inverter penetration on system stability for different unit configuration, with inclusion of transmission line dynamics. Transparent lines indicate results for scenarios without line dynamics.

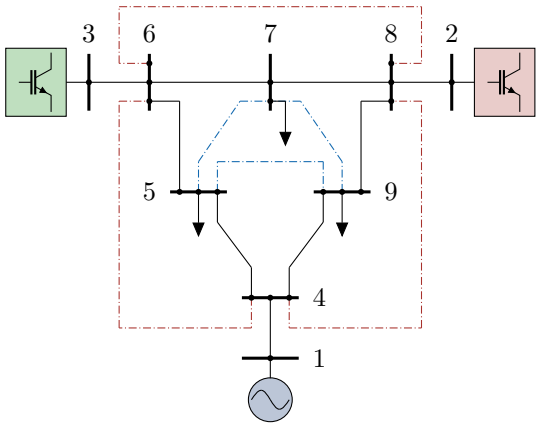

Fig. 13: Diagram of the IEEE 9-bus system. The blue and red lines indicate the additionally incorporated transmission lines.

solely to the AVR and PSS control design. The predominant impact of SMs on the system stability is even higher in Scenario II, with *grid-forming* inverters only marginally affecting the critical modes within a narrow range of $\eta \in [78, 79]$ %. Hence, the maximum admissible VSC penetration after the inclusion of transmission lines remains the same in this case.

D. Stability Margins of the IEEE 9-bus System

In order to investigate the simultaneous interactions between all three unit types, as well as to increase the network complexity, the IEEE 9-bus system presented in Fig. 13 is considered in this case study. The converter-based generation is placed at nodes 2 and 3, with a *grid-following* VSC being the former and a *grid-forming* the latter one. The transmission line dynamics are also included in the model.

The stability mapping for the IEEE 9-bus system is showcased in Fig. 14, while simultaneously considering different levels of network connectivity. Each triangular axis denotes a penetration of the respective unit type, more precisely η_{SG} refers to synchronous generators, η_F to *grid-forming* and η_f to *grid-following* inverter-based units. We modify the original system by gradually adding transmission lines, first between the generator buses and subsequently between the load buses, as indicated by the red and blue lines in Fig. 13 respectively. Such procedure allows us to increase the network connectivity, defined as $\varepsilon_g = 2N_b/(N_n^2 - N_n)$, from 40 % in the original model to 60 % and 80 % in the modified system.

It can be observed in Fig. 14 that there exists a minimum required level of synchronous generation in order to preserve system stability. For $\varepsilon_g = 40$ % this amounts to approximately 57 %, whereas for more meshed networks this limit can be reduced by 8−10 %. Nonetheless, it is clear that the production portfolios involving high penetration of converter-interfaced generation can drastically distort the system, independent of the *grid-forming* share. Interestingly, the permissible VSC installation margin significantly reduces when η_F/η_f ratio diverges from 1, as maximum value of $\eta = \eta_F + \eta_f$ drops from 44 % to 27 % in case of $\eta_F \approx 0$ % or $\eta_f \approx 0$ %. This is justified by different instabilities occurring between various unit types, specifically voltage issues for a system comprised of synchronous and inverter-based generators (Scenarios I and II) and synchronization obstacles related to a 100 % PE-based system (Scenario III), as described in Section V-B. For a rather balanced portfolio, all of these problems are somewhat confined within reasonable limits, while an imbalance in η_F/η_f ratio tends to emphasize the voltage instability and endanger the whole network. Another valid point can be made regarding the beneficial impact of transmission line dynamics. As previously indicated in Section V-C, a direct connection between units experiencing frequency instability mitigates the synchronization issues, thus facilitating a higher share of PE-based devices. Nonetheless, this is not the case for transmission lines between the load nodes, as increasing connectivity from 60 % to 80 % has a marginal impact on the stability margin.

We extend this analysis by differentiating between three different generation portfolios: (i) $\mathcal{P}_0$ - a mix of all three unit types, as previously discussed; (ii) $\mathcal{P}_f$ - a system comprised only of synchronous generators and *grid-following* VSCs; and (iii) $\mathcal{P}_F$ - a system comprised only of synchronous generators and *grid-forming* VSCs; in the latter two cases, the total inverter penetration ratio is equal to either η_f or η_F. The results for the IEEE 9-bus system presented in Fig. 15 suggest that more homogeneous portfolios, such as $\mathcal{P}_f$ and $\mathcal{P}_F$, can

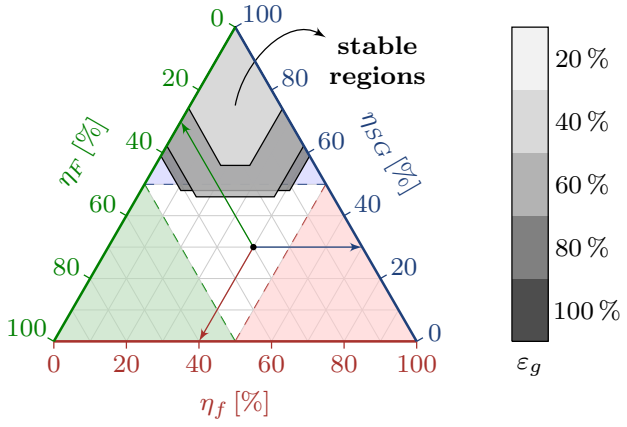

Fig. 14: Stability mapping for the IEEE 9-bus test case under different levels of network connectivity. Colored arrows indicate the appropriate reading on the respective axes.

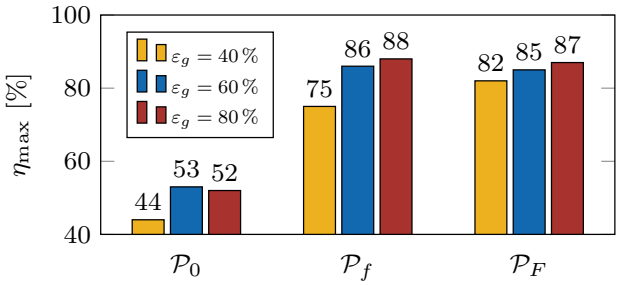

Fig. 15: Maximum permissible inverter penetration under different system portfolios ($\mathcal{P}$) and levels of network connectivity (ε_g).

withstand drastically higher penetration of renewables, with $\eta_{\max}$ reaching up to $75\,\%$ and $82\,\%$ respectively. Understandably, portfolio $\mathcal{P}_F$ has a higher η margin due to less accentuated voltage instability compared to $\mathcal{P}_f$ scenario. However, increasing network connectivity balances these penetration ratios out, as direct transmission line connections resolve the timescale separation between the voltage controllers of synchronous and converter-based generators (see Fig. 4). As a result, the system can facilitate up to $\eta_{\max} = 88\,\%$ of PE-interfaced units; an increase of approximately $70\,\%$ compared to the original portfolio $\mathcal{P}_0$.

E. Key Takeaway Messages

It should be noted that the obtained permissible penetration levels of inverter-based generation might vary drastically between systems of different sizes and complexity. While presented results should be taken with caution from a quantitative perspective, they highlight some important qualitative properties of future low-inertia systems. Therefore, several key conclusions can be drawn from this study:

1) Transition might be hard: The existing literature focuses mostly on 100% inverter-based power systems and the associated frequency stability and synchronization issues, assuming an easy transition along the way. While this might be the case from the perspective of stiff frequency signal in the network, the overall stability of the interim system is significantly more vulnerable and harder to ensure, as was already experienced in South Australian grid [12]. Although some solutions for fast frequency control have already been proposed [29], this is just a temporary mitigation of a much deeper and more convoluted problem, which as such should receive an adequate attention.

2) Need for uniform regulation: Throughout this study we assume a perfectly balanced converter control design, i.e., compatible control schemes and parameter tuning which ensure stable synchronization and safe operation of the system. However, this might not be the case in the future, especially considering current grid codes and lack of a uniform regulation for VSC manufacturers. As a matter of fact, the portfolios $\mathcal{P}_f$ and $\mathcal{P}_F$ could have even underperformed compared to $\mathcal{P}_0$ under such circumstances. Furthermore, even the sole definition and classification of converter operation modes, e.g., *grid-forming*, *grid-following* and *grid-supporting*, lacks foundation and tends to drastically differentiate between different operators and industries.

3) Timescale separation: One of the main contrasts between traditional and low-inertia systems is a timescale separation between the respective controllers of synchronous and inverter-based generators, which leads to frequency and voltage instabilities under high penetration of renewables. Due to significantly faster dynamics of VSCs, the conventional power systems are facing challenges in accommodating a predominantly high level of PE-interfaced units, especially in the case of very heterogeneous[1] production portfolios.

4) Premise of line dynamics: Transmission line dynamics have traditionally been neglected in power system studies, since their fast dynamics did not influence the dynamic behavior of the overall slower generation side. Nonetheless, with the introduction of fast-acting PE devices, the aforementioned interactions become drastically more profound in networks with low rotational inertia. Interestingly enough, they can have both positive and adverse effects on the system. On the one hand, the time constants of transmission lines enable them to act as a buffer and "bypass" the gap between fast inverter and slow SG dynamics, thus aiding system stability. Furthermore, direct line connections improve synchronization between generators. On the other, they impose strict upper bounds on droop feedback gains in order to ensure both voltage and frequency stability, which are not necessarily met by today's manufacturers. The latter property is especially pronounced in distribution networks, due to shorter node distances and a lower X/R line impedance ratio.

VI. Conclusion

The presented paper introduces a uniform, high-fidelity DAE formulation of a generic, low-inertia system that captures all relevant physical properties and associated dynamics. By combining detailed control schemes of both synchronous and converter-based generators, as well as the dynamics of loads and transmission lines, we determine the most vulnerable segments of the system and investigate the adverse effects of the underlying control interference. As a result, some new insights on the overall stability of low- and no-inertia systems are presented, together with the appropriate directions for improving the system stability margin under different generation portfolios. Furthermore, we clarify the issues related to timescale separation and the impact of line dynamics, and highlight the main obstacles in a transition from a traditional SG-based power system to the one with with almost no conventional generators.

Appendix A

Let us consider a set $j \in \mathcal{J}$ of interconnected grid-forming inverters with the active power control of the form:

$$\tau_z \dot{\omega}_{c_j} = \omega^*_{c_j} - \omega_{c_j} + R_p \left(p^*_{c_j} - p_{c_j} \right) \tag{41}$$

where $\tau_z = \omega_z^{-1}$ is the LPF time constant and the remaining notation is preserved from Section II. Having in mind that $\dot{\theta}_{c_j} = \omega_{c_j} \omega_b$, one can transform (41) into

$$\tau_z \ddot{\theta}_{c_j} = -\dot{\theta}_{c_j} + \omega_b \omega^*_{c_j} + \omega_b R_p \left(p^*_{c_k} - p_{c_k} \right) \tag{42}$$

[1]By heterogeneous we consider portfolios comprised of both *grid-forming* and *grid-following* VSCs, in addition to synchronous generators

The inverter output power p_{c_j} can be described as the sum of all powers flowing across the lines connecting the adjacent inverters $k \in \mathcal{K}_j$:

$$p_{c_j} = \sum_{k \in \mathcal{K}_j} p_{jk} = \sum_{k \in \mathcal{K}_j} \Re(\boldsymbol{v}_{c_j} \boldsymbol{i}_{jk}^*) \tag{43}$$

with $\boldsymbol{i}_{jk}$ being the complex vector of the current flowing through the line between inverters j and k, and $\theta_{jk} = \theta_{c_j} - \theta_{c_k}$ Furthermore, considering line parameters of the form (r_l, l_l), we express the electromagnetic dynamics of the line current in a (dq)-frame as

$$\dot{\boldsymbol{i}}_{jk} = \frac{\omega_b}{l_l}(\boldsymbol{v}_{c_j} - \boldsymbol{v}_{c_k}) - \left(\frac{r_l}{l_l}\omega_b + j\omega_b\omega_0\right)\boldsymbol{i}_{jk} \tag{44}$$

which is subsequently transformed into a Laplace domain:

$$\boldsymbol{i}_{jk} = \frac{\boldsymbol{v}_{c_j} - \boldsymbol{v}_{c_k}}{r_l + j\omega_0 l_l + s l_l/\omega_b} = \frac{\boldsymbol{i}_{jk}^0}{1 + \underbrace{s l_l / \left(\omega_0 r_l + j\omega_0^2 l_l\right)}_{\sigma_l}} \tag{45}$$

For the purposes of capturing the slow modes dynamics, it is reasonable to assume that $\sigma_l \ll 1$ holds for modes evolving on the timescales slower than the line time constant [28]. By performing a Taylor series expansion we obtain:

$$\begin{aligned} \boldsymbol{i}_{jk} &\approx \boldsymbol{i}_{jk}^0 - \frac{s l_l}{\omega_0 r_l + j\omega_0^2 l_l}\boldsymbol{i}_{jk}^0 \overset{\mathcal{L}^{-1}}{\longmapsto} \\ \boldsymbol{i}_{jk} &\approx \boldsymbol{i}_{jk}^0 - \frac{l_l}{\omega_0 \left(r_l + j\omega_0 l_l\right)^2}\left(\dot{\boldsymbol{v}}_{c_j} - \dot{\boldsymbol{v}}_{c_k}\right) \end{aligned} \tag{46}$$

Assuming nominal voltage magnitudes and small angle deviations between the nodes ($v_{c_{j,k}} \approx 1\,\text{p.u.}$, $\theta_{jk} \approx 0$), we can compute the time derivatives of voltage phasors and subsequently the total active power injection:

$$\begin{aligned} p_{c_j} &= \sum_{k \in \mathcal{K}_j} \left(\frac{\omega_0 l_{jk}}{\left(r_{jk}^2 + \omega_0^2 l_{jk}^2\right)^2}\theta_{c_j} + \frac{2 r_{km} l_{km}^2}{\left(r_{km}^2 + \omega_0^2 l_{km}^2\right)^2}\dot{\theta}_{c_j} \right) \\ &= B_j \theta_{c_j} + B_j' \dot{\theta}_{c_j} \end{aligned} \tag{47}$$

where subscript jk denotes the respective parameters (r_l, l_l) of the power line connecting the nodes j and k. Combining (41) and (47) yields the uniform frequency dynamics of an individual inverter of the form:

$$\tau_z \ddot{\theta}_{c_j} + \left(1 - \omega_b R_p B_j'\right)\dot{\theta}_{c_j} + \omega_b R_p B_j \theta_{c_j} + C_j = 0 \tag{48}$$

with $C_j = \omega_b \omega_{c_j}^* + \omega_b R_p p_{c_j}^*$.

REFERENCES

[1] F. Milano, F. Dörfler, G. Hug, D. J. Hill, and G. Verbič, "Foundations and challenges of low-inertia systems," in *Power Systems Computation Conference (PSCC)*, Jun 2018.

[2] P. Kundur, *Power System Stability and Control*. McGraw-Hill, 1994.

[3] J. Machowski, J. W. Bialek, and J. R. Bumby, *Power System Dynamics: Stability and Control*. Wiley, 2008.

[4] S. D'Arco, J. A. Suul, and O. B. Fosso, "Small-signal modelling and parametric sensitivity of a virtual synchronous machine," in *2014 Power Systems Computation Conference*, Aug 2014.

[5] U. Markovic, J. Vorwerk, P. Aristidou, and G. Hug, "Stability analysis of converter control modes in low-inertia power systems," in *2018 IEEE Innovative Smart Grid Technologies - Europe (ISGT-Europe)*, Oct 2018.

[6] U. Markovic, O. Stanojev, P. Aristidou, and G. Hug, "Partial grid forming concept for 100% inverter-based transmission systems," in *IEEE PES General Meeting*, Aug 2018.

[7] N. Pogaku, M. Prodanovic, and T. C. Green, "Modeling, analysis and testing of autonomous operation of an inverter-based microgrid," *IEEE Transactions on Power Electronics*, vol. 22, no. 2, pp. 613–625, March 2007.

[8] J. Schiffer, R. Ortega, A. Astolfi, J. Raisch, and T. Sezi, "Conditions for stability of droop-controlled inverter-based microgrids," *Automatica*, vol. 50, no. 10, pp. 2457 – 2469, 2014.

[9] S. Leitner, M. Yazdanian, A. Mehrizi-Sani, and A. Muetze, "Small-signal stability analysis of an inverter-based microgrid with internal model-based controllers," *IEEE Transactions on Smart Grid*, vol. 9, no. 5, pp. 5393–5402, Sep. 2018.

[10] EirGrid and SONI, "DS3: System services review TSO recommendations," EirGrid, Tech. Rep., May 2013.

[11] J. Matevosyan and P. Du, "Wind integration in ERCOT," in *Integration of Large-Scale Renewable Energy into Bulk Power Systems*. Springer, 2017, pp. 1–25.

[12] Australian Energy Market Operator, "Black System South Australia 28 September 2016 - Final Report," Tech. Rep., March 2017.

[13] S. D'Arco and J. A. Suul, "Small-signal analysis of an isolated power system controlled by a virtual synchronous machine," in *2016 IEEE International Power Electronics and Motion Control Conference (PEMC)*, Sep. 2016, pp. 462–469.

[14] F. Katiraei, M. R. Iravani, and P. W. Lehn, "Small-signal dynamic model of a micro-grid including conventional and electronically interfaced distributed resources," *IET Generation, Transmission Distribution*, vol. 1, no. 3, pp. 369–378, May 2007.

[15] Y. Lin, B. Johnson, V. Gevorgian, V. Purba, and S. Dhople, "Stability assessment of a system comprising a single machine and inverter with scalable ratings," in *2017 North American Power Symposium (NAPS)*, Sep. 2017, pp. 1–6.

[16] D. Li, Q. Zhu, S. Lin, and X. Y. Bian, "A self-adaptive inertia and damping combination control of vsg to support frequency stability," *IEEE Transactions on Energy Conversion*, vol. 32, no. 1, pp. 397–398, March 2017.

[17] S.-K. Chung, "A phase tracking system for three phase utility interface inverters," *IEEE Transactions on Power Electronics*, vol. 15, no. 3, pp. 431–438, May 2000.

[18] H. P. Beck and R. Hesse, "Virtual synchronous machine," in *2007 9th International Conference on Electrical Power Quality and Utilisation*, Oct 2007.

[19] J. Driesen and K. Visscher, "Virtual synchronous generators," in *2008 IEEE Power and Energy Society General Meeting - Conversion and Delivery of Electrical Energy in the 21st Century*, July 2008.

[20] R. Ofir, U. Markovic, P. Aristidou, and G.Hug, "Droop vs. virtual inertia: Comparison from the perspective of converter operation mode," in *2018 IEEE International Energy Conference (ENERGYCON)*, June 2018.

[21] X. Wang, Y. W. Li, F. Blaabjerg, and P. C. Loh, "Virtual-impedance-based control for voltage-source and current-source converters," *IEEE Transactions on Power Electronics*, vol. 30, no. 12, pp. 7019–7037, Dec 2015.

[22] S. D'Arco, J. A. Suul, and O. B. Fosso, "Virtual synchronous machines - classification of implementations and analysis of equivalence to droop controllers for microgrids," in *2013 IEEE Grenoble Conference*, June 2013.

[23] Y. Lin, B. Johnson, V. Gevorgian, V. Purba, and S. Dhople, "Stability assessment of a system comprising a single machine and inverter with scalable ratings," in *2017 North American Power Symposium (NAPS)*, Sept 2017.

[24] ENTSO-E, "Documentation on controller tests in test grid configurations," Tech. Rep., November 2013.

[25] C. Spanias and I. Lestas, "A system reference frame approach for stability analysis and control of power grids," *ArXiv e-prints*, Sep. 2018.

[26] P. Vorobev, P. Huang, M. A. Hosani, J. L. Kirtley, and K. Turitsyn, "A framework for development of universal rules for microgrids stability and control," in *2017 IEEE 56th Annual Conference on Decision and Control (CDC)*, Dec 2017.

[27] D. Groß, M. Colombino, J.-S. Brouillon, and F. Dörfler, "The effect of transmission-line dynamics on grid-forming dispatchable virtual oscillator control," *ArXiv e-prints*, Feb. 2018.

[28] P. Vorobev, P. Huang, M. A. Hosani, J. L. Kirtley, and K. Turitsyn, "High-fidelity model order reduction for microgrids stability assessment," *IEEE Transactions on Power Systems*, vol. 33, no. 1, pp. 874–887, Jan 2018.

[29] Australian Energy Market Operator, “Initial operation of the Hornsdale Power Reserve Battery Energy Storage System,” Tech. Rep., April 2018.